THE ASTROPHYSICAL JOURNAL, 532:980–993, 2000 April 1

MOLECULAR CLOUD FORMATION IN SHOCK-COMPRESSED LAYERS

HIROSHI KOYAMA[1] AND SHU-ICHIRO INUTSUKA
Division of Theoretical Astrophysics, National Astronomical Observatory, Mitaka, Tokyo 181-8588, Japan; hkoyama@th.nao.ac.jp, inutsuka@th.nao.ac.jp
Received 1999 May 3; accepted 1999 November 17

ABSTRACT

We investigate the propagation of a shock wave into a warm neutral medium and a cold neutral medium by one-dimensional hydrodynamic calculations with detailed treatment of thermal and chemical processes. Our main result shows that thermal instability inside the shock-compressed layer produces a geometrically thin, dense layer in which a large amount of hydrogen molecules are formed. Linear stability analysis suggests that this thermally collapsed layer will fragment into small molecular cloudlets. We expect that frequent compression due to supernova explosions, stellar winds, spiral density waves, etc., in the Galaxy causes the interstellar medium to be occupied by these small molecular cloudlets.

Subject headings: instabilities — ISM: clouds — ISM: molecules — shock waves — supernova remnants

1. INTRODUCTION

The tiny-scale structures on scales of tens of astronomical units were observed in the interstellar medium (ISM). These structures have been detected by 21 cm absorption lines against quasars with VLBI techniques (Dieter, Welch, & Romney 1976), against pulsars with time variability (Frail et al. 1994), and against close binary stars in optical interstellar lines (Meyer & Blades 1996). The tiny-scale structure is seen in all directions for which it has been searched, which suggests that it is ubiquitous, not associated with large extinction (Heiles 1997). AU-sized structures have been seen not only in atomic gas but also in molecular gas. Langer et al. (1995) observed several clumps ranging in size from 0.007 to 0.021 pc in the Taurus molecular cloud 1 with interferometer techniques. The mass of these smallest fragments is of the order of 0.01 $M_\odot$. These small-scale structures appear to be gravitationally unbound by a large factor. The presence of these tiny-scale atomic and molecular structures in a variety of ISM suggests that their formation mechanisms have some similarities.

Models of the ISM have been studied by many authors. Field, Goldsmith, & Habing (1969) first showed that a cold ($T \sim 50$ K) neutral medium (CNM) and a warm ($T \sim 8000$ K) neutral medium (WNM) can be in pressure equilibrium. Cox & Smith (1974) showed that supernova explosions can greatly modify the general aspect of the ISM. McKee & Ostriker (1977) developed a theory of a supernova-dominated ISM. The late-phase supernova remnant (SNR) expands until the internal pressure drops to the ambient interstellar pressure ($n = 0.1$ cm^{-3}, $T = 10^4$ K). This maximum radius $R_{\max} = 10^{2.1}$ pc is reached at a time $t_{\max} = 10^{6.3}$ yr. The total volume $SR_{\max}^3 t_{\max}$ which all SNRs occupy in the maximum expansion time $t_{\max}$ exceeds the volume of the Galactic disk, where $S \sim 10^{-2}$ yr^{-1} is the supernova rate in our Galaxy. This means that the SNRs overlap before they are dissipated. Thus, the study of shock propagation into the ISM is important.

In this paper, we study the basic processes in the evolution of the ISM with a strong shock wave by means of one-dimensional hydrodynamic calculations with nonequilibrium thermal and chemical processes. The processes we include in our calculations are photoelectric heating from small grains and polycyclic aromatic hydrocarbons (PAHs), heating and ionization by cosmic rays and X-rays, heating by H_2 formation and destruction, atomic line cooling from hydrogen Lyα, C II, O I, Fe II, and Si II, rovibrational line cooling from H_2 and CO, and atomic and molecular collisions with grains. Effects of self-gravity and the magnetic field are not treated in this paper. In the next section, we explain the details of our numerical methods. Results are presented in § 3. In § 4, we discuss the formation of small molecular cloudlets. Section 5 presents a summary.

2. NUMERICAL METHODS

2.1. *Hydrodynamic Equations*

To study the thermal and dynamical evolution of a shock-compressed layer, we use a one-dimensional plane-parallel numerical method. The hydrodynamics module of our scheme is based on the second-order Godunov method. We use the result of Riemann problem at each cell interface to calculate numerical fluxes without introducing any artificial viscosity, which characterizes the Godunov method. A higher order Godunov method has been the state-of-the-art numerical method in last two decades (see, e.g., van Leer 1997) and widely used in an astrophysical context (see, e.g., Truelove et al. 1998). The hydrodynamic equations for the system are written as follows:

$$\frac{d\rho}{dt} + \rho \frac{\partial v}{\partial X} = 0 , \tag{1}$$

$$\rho \frac{dv}{dt} = -\frac{\partial P}{\partial X} , \tag{2}$$

$$P = \left(1.1 + x_e - \frac{x_2}{2}\right) n k_B T , \tag{3}$$

$$\rho = 1.4 m_H n , \tag{4}$$

$$\frac{1}{\gamma - 1}\frac{dP}{dt} - \frac{\gamma}{\gamma - 1}\frac{P}{\rho}\frac{d\rho}{dt} = n\Gamma - n\Lambda + \frac{\partial}{\partial X} K \frac{\partial T}{\partial X} . \tag{5}$$

In the above equations, n is the number density of hydrogen nuclei, ρ is the mass density of the gas, v is the velocity of fluid elements, P is the gas pressure, and K is the coefficient of thermal conductivity. We have assumed an abundance of He atoms is $0.1n$. For the range of temperatures and ionized fractions considered, the dominant contribution to thermal conductivity is that due to neutral atoms, for which

[1] Also at the Department of Astronomy, School of Science, University of Tokyo, Bunkyo-ku, Tokyo 113-0033, Japan.

$K = 2.5 \times 10^3 T^{1/2}$ cm^{-1} K^{-1} s^{-1} (Parker 1953). We use the ratio of the specific heats $\gamma = 5/3$ for simplicity. The values of Γ and Λ are the heating and cooling rate per hydrogen nucleus, respectively. These rates depend on number density n, temperature T, electron fraction $x_e = n(e^-)/n$, H_2 fraction $x_2 = 2n(H_2)/n$, and CO fraction $x_{CO} = n(CO)/n$. The gas behind the shock front is in a chemical nonequilibrium state. Therefore, we solve three chemical equations for x_e, x_2, and x_{CO} and hydrodynamic equations simultaneously.

2.2. *Heating and Cooling Processes*

Wolfire et al. (1995, hereafter W95) calculated the thermal equilibrium state in the neutral atomic phase. We follow their calculation for $n < 10^3$ cm^{-3}. We also calculate molecular processes for 10^3 cm$^{-3} < n < 10^6$ cm^{-3} (see Fig. 1). Contributions to the heating of an interstellar cloud are from the photoelectric emission from small grains and PAHs, ionization by cosmic rays and soft X-rays, and the formation and photodissociation of H_2. Following W95, the local far-ultraviolet (FUV) field is set to 1.7 times Habing's estimate (i.e., $G_0 = 1.7$). The cooling function is dominated by line emission from H, C, O, Si, and Fe, by rovibrational lines from H_2 and CO, and by atomic and molecular collisions with dust grains. To solve these thermal processes in nonequilibrium, we solve a set of three time-dependent equations for the ionization and recombination of hydrogen and for the formation and dissociation of H_2 and CO. Self-shielding effects are also included in the calculation of H_2 photodissociation. The details of these processes are presented in Appendix A. Figure 1 shows the equilibrium temperature, pressure, and chemical fractions as functions of number density. Important physical timescales are also shown in Figure 1.

2.3. *Initial and Boundary Conditions*

The strong shock wave is characterized by the Mach number. To analyze the evolution of ISM swept up by a strong shock wave, we set up a plane-parallel cloud which collides against a rigid wall. Figure 2 shows the schematic configuration of our calculation. This configuration also corresponds to a face-on collision between two identical clouds.

We have generated a grid of calculations for varying initial densities and collision velocities. The typical models are summarized in Table 1. Initial temperatures and chemical fractions are taken to be the value of the thermal and chemical equilibrium state (see Fig. 1). The velocity differ-

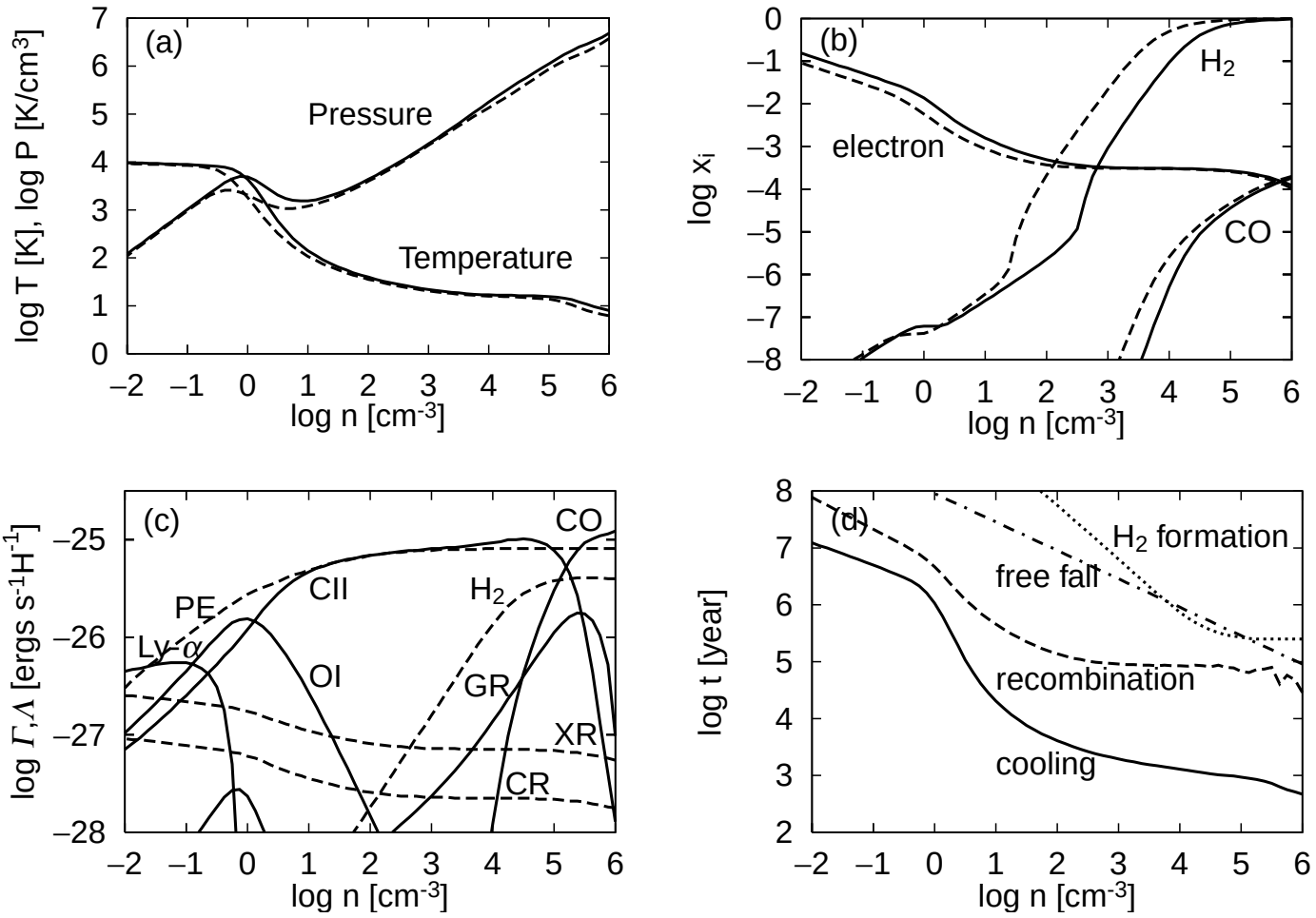

FIG. 1.—(*a*) Equilibrium temperature and pressure. An absorbing column is 10^{19} cm^{-2} (*solid lines*), 10^{20} cm^{-2} (*dashed lines*). (*b*) Chemical fractions as functions of number density. (*c*) Heating (*dashed lines*) and cooling (*solid lines*) rates per hydrogen nucleus in equilibrium condition corresponding to panel (*a*) (*solid lines*). Heating processes are photoelectric from small grains and PAHs (PE), X-ray (XR), cosmic ray (CR), and H_2 formation/destruction (H_2). Cooling processes are C II fine-structure (CII), O I fine-structure (OI), hydrogen Lyα (Ly-α), CO rotation/vibration line (CO), and atomic and molecular collisions with dust grains (GR). (*d*) Comparison of various timescales, cooling time (*solid line*), recombination time (*dashed line*), free-fall time (*dot-dashed line*), and H_2 formation time (*dotted line*), which is defined by $(Rn_{H_I})^{-1}$.

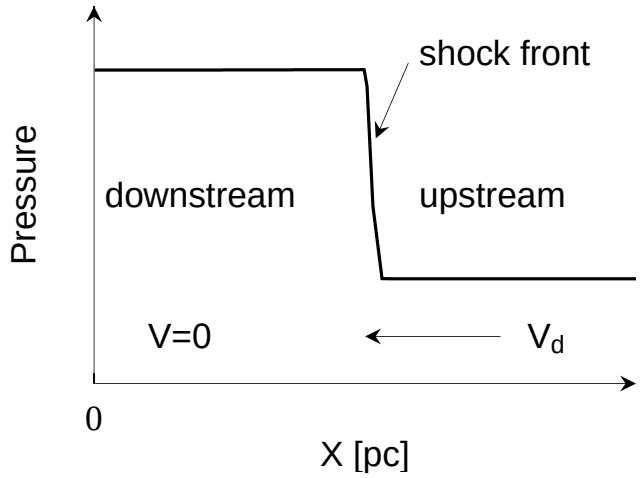

FIG. 2.—Schematic configuration of our calculation. The shock front propagates from left to right. The velocity difference, V_d, is defined by upstream velocity minus downstream velocity which we set to be zero.

ence, V_d, defined by upstream velocity minus downstream velocity, corresponds to the range of the Mach number $M = 2$–12. This range of Mach number in the WNM ($T \sim 8000$ K) corresponds to the sweeping-up speed of momentum-driven SNRs. External FUV and X-ray radiation penetrate from both sides of two identical clouds. The extinction of the radiation is evaluated by the cumulative column density of each grid. The largest total column density we considered is that of the standard H I cloud (10^{19}–10^{20} cm^{-2}).

3. RESULTS

3.1. *Shock Propagation into WNM*

In this section, we analyze the model W6, where a shock wave propagates into WNM. Figure 3 shows the result of the calculation. Snapshots at $t = 8.0 \times 10^4$, 1.3×10^5, 2.5×10^5, and 2.9×10^6 yr are shown. The horizontal axis in logarithmic scale denotes the distance from the rigid wall. Figure 3*a* shows the evolution of pressure. The shock-compressed layer is almost isobaric. The shock front propagates from left to right. Figure 3*b* shows the evolution of temperature. Lyα cooling is so efficient that the temperature of postshock gas quickly decreases to the preshock value. In § 3.2, we analyze the shock front in detail. Behind the shock front, cooling dominates heating because the density is larger and temperature decreases monotonically. Around $t \simeq 10^5$ yr, temperature starts to decline rapidly because of thermal instability. This instability is mainly driven by O I (63 μm) and C II (157 μm) line cooling. Eventually temperature attains a thermal equilibrium value $T \simeq 19$ K at $n \simeq 2.5 \times 10^3$ cm^{-3}. The main coolant of the collapsed layer is C II (see Fig. 1*c*). Figure 3*c* shows the evolution of number density. A thin layer is formed by thermal instability in the shock-compressed layer. The width of the thermally collapsed layer is much shorter than the shock-compressed layer. However, the column density of the thermally collapsed layer becomes comparable after $t = 2.6 \times 10^5$ yr (Fig. 3*c*, *dotted line*). Figure 3*d* shows the evolution of velocity. Figure 3*e* shows the evolution of electron fraction. High shock temperature raises the ionization degree in the postshock gas. The timescale of recombination of electrons in the postshock layer is larger than the timescale of gas cooling. Figure 3*f* shows the evolution of the H_2 number fraction. Because the timescale of H_2 formation is much larger than cooling timescale (see Fig. 1*d*), this thermal instability is not driven by H_2 cooling. In the highest density region at the final time step (*dot-dashed line*), 1.3% of the hydrogen is in H_2 and 0.0002% of the carbon is in CO. Note that the preshock H_2 number fraction at the final time step (*dot-dashed line*) is larger than the initial fraction because H_2 photodissociation radiation from the left-hand side is shielded by large H_2 column density in the collapsed layer in this one-dimensional plane-parallel model.

3.2. *Structure across the Shock Front*

In this subsection, we analyze the detailed structure across the shock front which propagates into the WNM. The same calculations as model W6 at $t = 1 \times 10^4$ are

TABLE 1

MODELS

Model	n_i[a]	T_i[b]	x_{ei}[c]	N_H[d]	M[e]	V_d[f]	t_f[g]	n_f[h]	T_f[i]	P_f/k_B[j]	x_{2f}[k]
W2	0.1	8491	0.03	1(20)[l]	2	18	7.0(6)	1.73	6353	3.3(3)	9.5(−8)
W6[m]	0.1	8491	0.03	1(20)	6	54	2.9(6)	2.5(3)	18.7	5.2(4)	0.013
W6L.....	0.1	8912	0.05	1(19)	6	54	2.8(5)	2.5(3)	19.0	5.2(4)	5.6(−5)
W12	0.1	8491	0.03	1(20)	12	109	1.45(6)	1.2(4)	16.6	2.0(5)	0.21
I12.....	0.1	8491	1.00	1(20)	12	109	1.45(6)	1.2(4)	16.6	2.0(5)	0.21
C2	10	107	8.7(−4)	1(20)	2	2.1	7.0(5)	2.8(2)	28.5	8.8(3)	5.1(−5)
C10[n]	10	107	8.7(−4)	1(20)	10	10	1.0(5)	1.4(4)	16.7	2.5(5)	0.049

[a] The initial number density of hydrogen nuclei in cm^{-3}.
[b] The initial temperature in K.
[c] The initial electron fraction.
[d] The total column density of hydrogen nuclei in cm^{-2}.
[e] The Mach number in the center of mass frame.
[f] The velocity difference in km s^{-1}, defined by upstream velocity minus downstream velocity which we set to be zero.
[g] The final time in years.
[h] The maximum density in cm^{-3} at the final time step.
[i] The temperature in K in the maximum density regions at the final time step.
[j] The pressure in K cm^{-3} in the maximum density regions at the final time step.
[k] The H_2 fraction in the maximum density region at the final time step.
[l] The notation $a(b)$ means $a \times 10^b$.
[m] Details of this model are discussed in § 3.1.
[n] Details of this model are discussed in § 3.4.

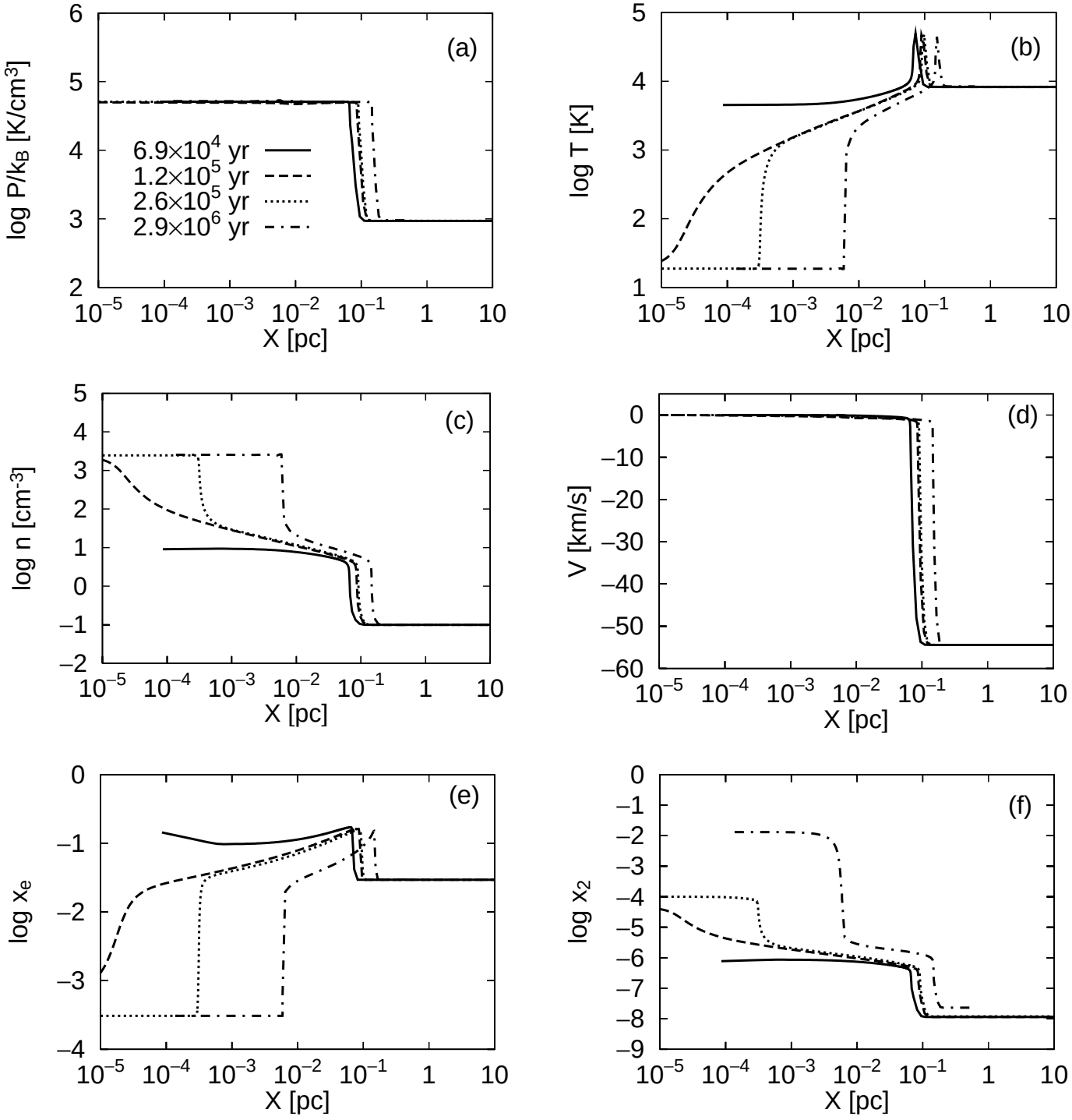

FIG. 3.—The evolution of the shock propagation into the WNM. The figures show (*a*) pressure, (*b*) temperature, (*c*) number density of hydrogen nuclei, (*d*) velocity, (*e*) electron number fraction, and (*f*) H_2 number fraction. Solid lines denote the compressed layer at $t = 8.0 \times 10^4$ yr, dashed lines at $t = 1.3 \times 10^5$ yr, dotted lines at $t = 2.5 \times 10^5$ yr, and dot-dashed lines at $t = 2.9 \times 10^6$ yr.

shown in Figure 4. Dashed lines show the calculation which used the same initial grid spacing as model W6. We also calculated the model with 320 times higher spatial resolution (*solid lines*) to resolve detailed structure of the shock front. Dotted lines denote the same calculation without cooling and heating processes. The width of the shock front is on the order of the collision mean free path, $l = 1/n\sigma_{\rm col} \approx 0.0003/n$ pc. For a strong shock without cooling, postshock temperature is determined by the Rankine-Hugoniot relation as $T_2 = (\gamma - 1)mV_d^2/2k_{\rm B}$. On the other hand, shock temperature with cooling is estimated by the following equation:

$$\frac{k_{\rm B}\,T_s}{\gamma - 1} + E_{\rm loss} = \frac{1}{2}\,mV_d^2\,, \tag{6}$$

where $E_{\rm loss} = \int n(\Lambda - \Gamma)dt \approx n\Lambda_{{\rm Ly}\alpha}(T_s)l/V_d$. This analytic estimation provides $\log\, T_s[{\rm K}] = 4.8$ in this model. Even the lowest resolution model can provide the same values of physical quantities in the postshock region.

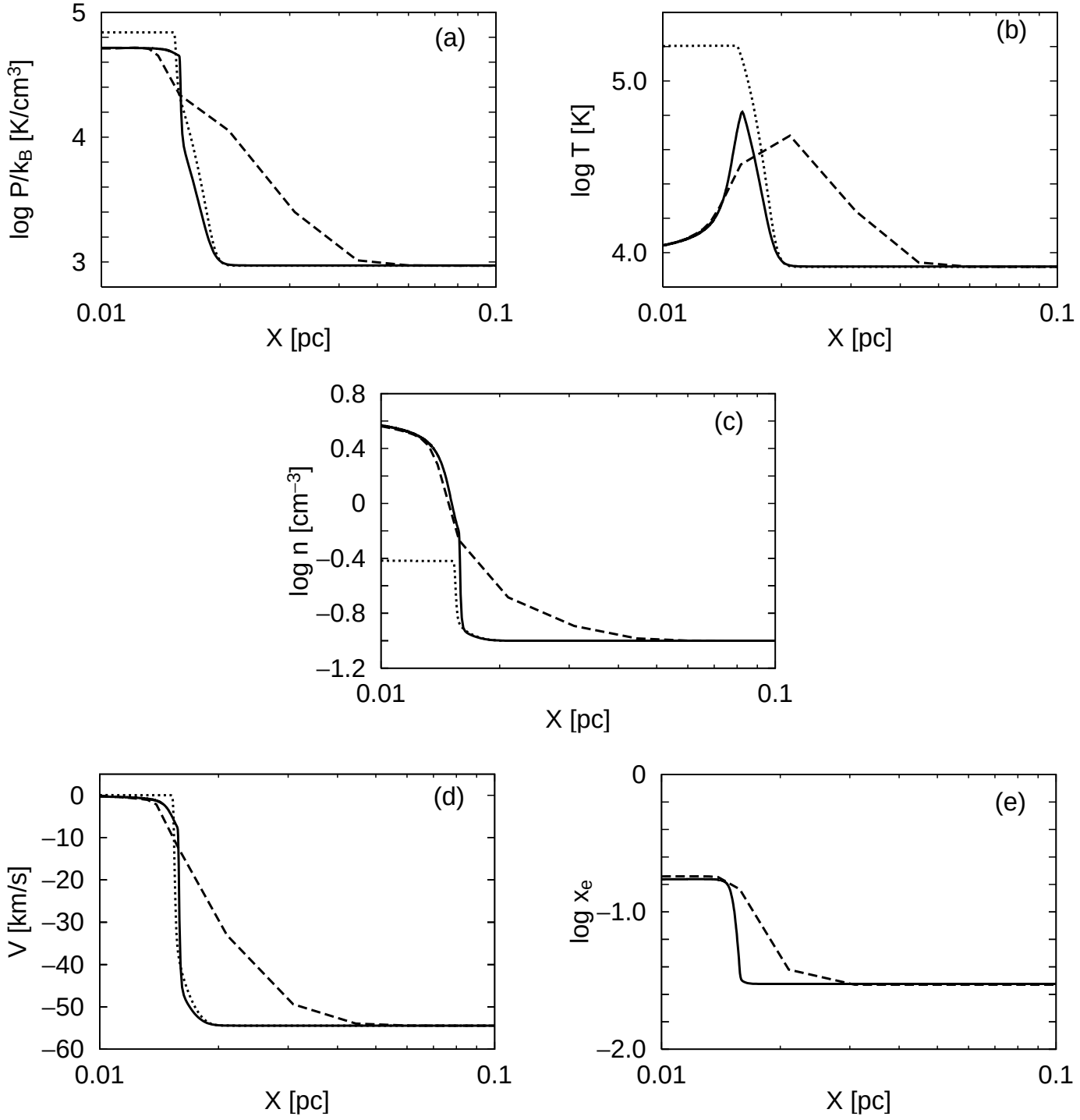

FIG. 4.—Structure across the shock front. The model W6 at $t = 1 \times 10^4$ yr is shown. The figures show (*a*) pressure, (*b*) temperature, (*c*) number density of hydrogen nuclei, (*d*) velocity, and (*e*) electron number fraction. Dashed lines correspond to the same spatial resolution as Fig. 3. Solid lines denote the calculation with 320 times higher spatial resolution than dashed lines. Dotted lines denote the calculation with 640 times higher resolution without cooling and heating.

Radiative precursor, which is not treated in our models, can change preshock temperature and ionization. Shull & McKee (1979) have calculated the ionization of the preshock gas which is caused by the diffuse radiation from the postshock gas in their models of interstellar shock waves with $v_s = 40$–130 km s^{-1}. They have concluded that sufficiently fast shocks ($v_s > 110$ km s^{-1}) completely ionize the preshock gas. To study this effect, we also calculated the model with fully ionized preshock gas (model I12) and found no significant difference between the models I12 and W12. Therefore, we neglect the effect of radiative precursor in the rest of this paper.

3.3. *Thermal Instability of Isobarically Cooling WNM*

Figure 5 shows the evolution of the fluid element which has the maximum density at each time step. Density, temperature, and pressure evolve on the dashed lines from left to right. Solid and thick lines correspond to the thermally stable equilibrium. Dotted lines correspond to the thermally unstable equilibrium. The preshock gas is a thermally

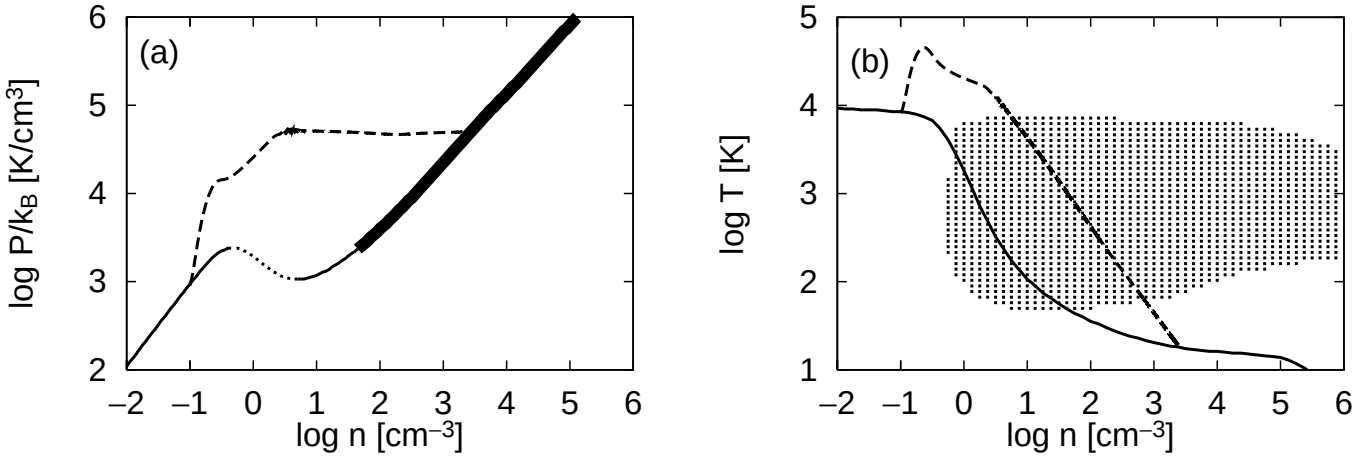

FIG. 5.—The evolution track of WNM compression on the n-P and n-T planes. Density, temperature, and pressure evolve on the dashed lines from left to right. Solid and thick lines correspond to the thermally stable equilibrium. Dotted lines correspond to the thermally unstable equilibrium. In Appendix B, we investigate the stability of isobarically contracting gas by linear perturbation theory to analyze the evolution on the dashed lines. (*b*) Shaded area denotes the thermally unstable region determined by the linear analysis. A larger electron fraction makes the cooling rate larger, so that the unstable region is wider than the unstable region of equilibrium gas. This shaded region predicts that thermal instability is inevitable when WNM cools into CNM.

stable WNM ($n = 0.1$ cm^{-3}, $T = 8000$ K). In Appendix B, we investigate the stability of isobarically contracting gas by linear perturbation theory to analyze the evolution on the dashed lines. We have used the postshock values of the hydrodynamic calculation as the chemical compositions in the linear analysis ($x_e = 0.1$, $x_2 = 10^{-6.3}$, $x_{\rm CO} = 10^{-23}$) because the chemical reaction timescale is longer than the cooling timescale. The shaded area in Figure 5*b* denotes the thermally unstable region determined by the linear analysis. The larger electron fraction makes the cooling rate larger, so that the unstable region is wider than the unstable region of equilibrium gas. This shaded region shows that thermal instability is inevitable when WNM cools into CNM.

Next, we discuss the characteristic length and timescale of the thermal instability. The linear growth rate of thermal instability as a function of perturbation wavelength is calculated with a given temperature and density. The growth time of the instability is shown in Figure 6. In this figure, the vertical axis denotes the unperturbed temperature. The value of the constant pressure, $P_c/k_{\rm B} = 5 \times 10^4$ K cm^{-3}, is adopted from the result of our nonlinear calculation. The density can be deduced from the relation $n = P_c/k_{\rm B}\,T$. The horizontal axis denotes a quarter of the perturbation wavelength. Contours of growth time are depicted in this wavelength-temperature plane. In Figure 6*b*, the temperature evolution of our nonlinear calculation (Fig. 3*b*) is superposed upon the growth rate contours (Fig. 6*a*). Thermal instability occurs at temperatures less than 7300 K. The instability becomes drastic at temperatures below 1000 K, which corresponds to the growth time less than 10^4 yr. In this way we can understand the collapse of the layer in terms of thermal instability. The shortest wavelength of unstable perturbation is $\lambda_{\rm min} \sim 8 \times 10^{-5}$ pc ≈ 16 AU. The thickness of the thermally collapsed layer increases with time through the accretion of gas.

3.4. *Shock Propagation into CNM*

In this section, we analyze the model C10, where shock wave propagates into CNM. Although Smith (1980) has done a similar calculation, his calculation does not have sufficient dynamic range to resolve the thermally collapsing

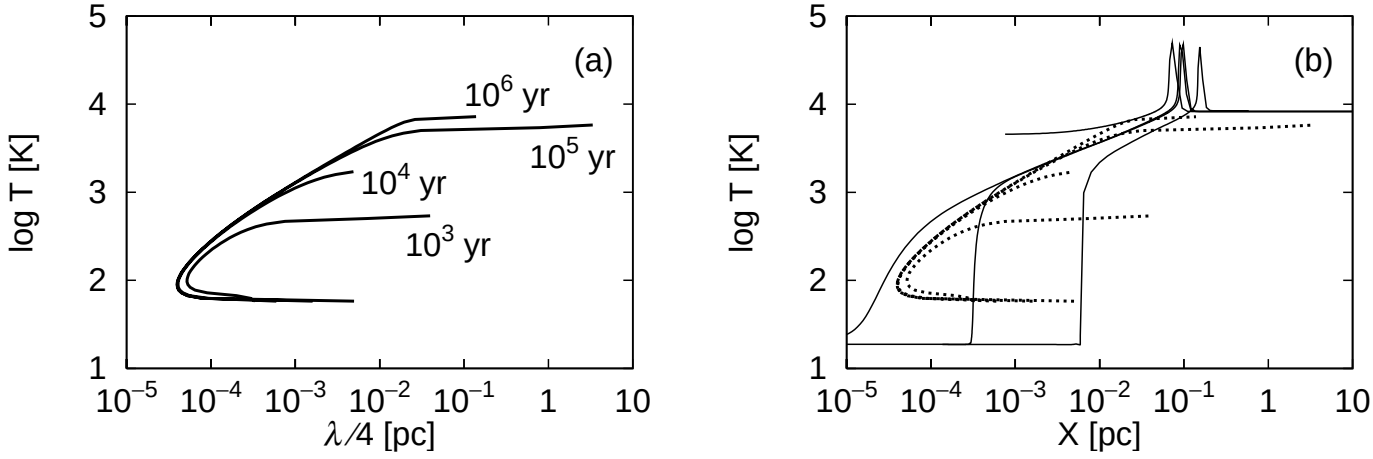

FIG. 6.—Growth time of the instability. The vertical axis denotes unperturbed temperature. The value of the constant pressure, $P_c/k_{\rm B} = 5 \times 10^4$ K cm^{-3}, is adopted from the result of our nonlinear calculation. The density can be deduced from the relation $n = P_c/k_{\rm B}\,T$. The horizontal axis denotes a quarter of the perturbation wavelength. Contours of growth time are depicted in this wavelength-temperature plane. The shortest wavelength of unstable perturbation is $\lambda_{\rm min} \sim 8 \times 10^{-5}$ pc ≈ 16 AU. (*b*) We superpose the temperature evolution of our nonlinear calculation (Fig. 3*b*) upon the growth rate contours shown in panel *a*.

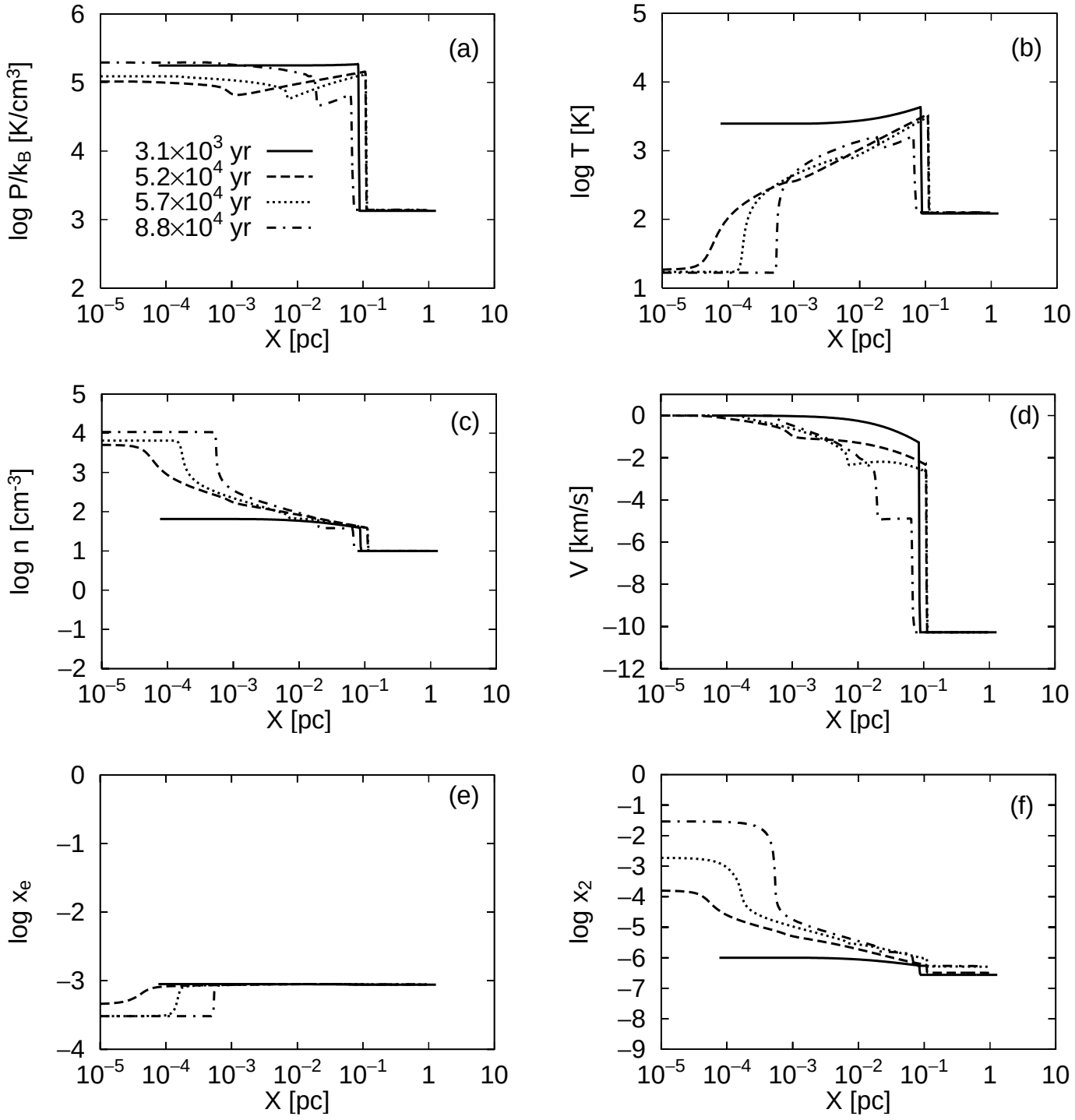

FIG. 7.—Evolution of the shock propagation into the CNM. The figures show (*a*) pressure, (*b*) temperature, (*c*) number density of hydrogen nuclei, (*d*) velocity, (*e*) electron number fraction, and (*f*) H_2 number fraction. Solid lines denote the compressed layer at $t = 3.1 \times 10^3$ yr, dashed lines at $t = 5.2 \times 10^4$ yr, dotted lines at $t = 5.7 \times 10^4$ yr, and dot-dashed lines at $t = 8.8 \times 10^4$ yr.

layer which is of our interest. Figure 7 shows the results of our calculation where the Mach number $M = 10$, which corresponds to the velocity difference of 10 km s^{-1}. Snapshots at $t = 3.1 \times 10^3$, 5.2×10^4, 5.7×10^4, and 8.8×10^4 yr are shown. The shock front is almost adiabatic. The postshock pressure can be estimated by the Rankine-Hugoniot relation as follows:

$$\frac{P_2}{P_1} = 1 + \frac{\gamma(\gamma+1)}{4} M^2 + \frac{\gamma}{4} M\sqrt{(\gamma+1)^2 M^2 + 16}\,, \quad (7)$$

where M is the Mach number in the center of mass frame. When M equals 10, the postshock pressure is 224 times higher than the ambient pressure. Details of postshock structure are more complicated than those in the WNM case. The postshock gas, of which temperature and density are determined by the adiabatic shock condition, is thermally unstable (see Fig. 8*b*). The shock front decelerates after the postshock layer collapses. After the thermally collapsed layer is formed, accretion shock is formed inside the shock-compressed layer. Accretion shock propagates into

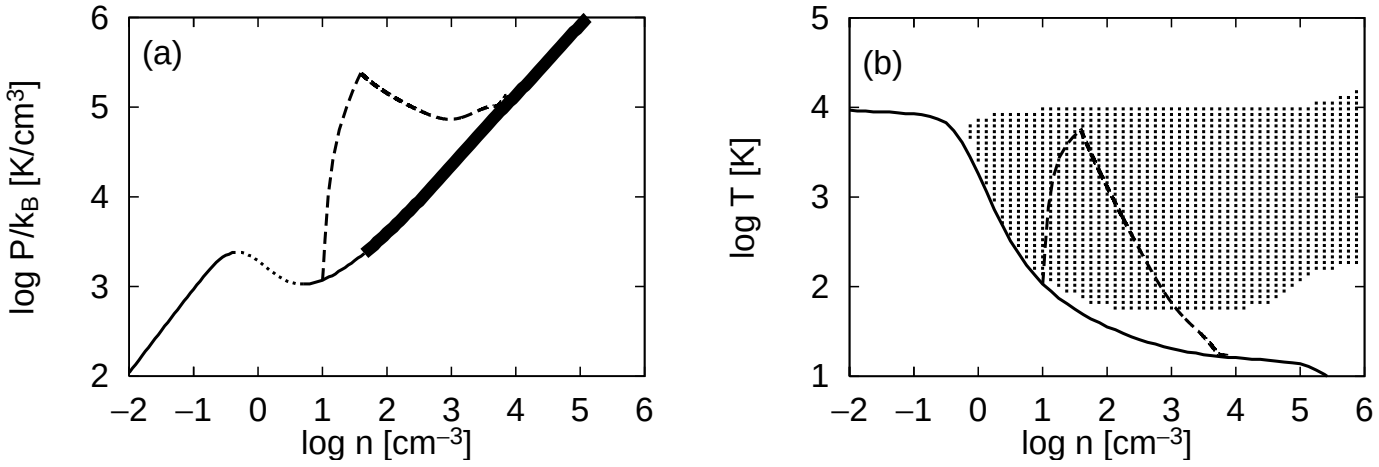

FIG. 8.—Evolution track of CNM compression on the n-P and n-T planes. Density, temperature, and pressure evolve on the dashed lines from left to right. Solid and thick lines correspond to the thermally stable equilibrium. Dotted lines correspond to the thermally unstable equilibrium. (*b*) Shaded area denotes thermally unstable region determined by the linear analysis. This figure shows how thermally stable CNM becomes unstable.

the compressed layer. In the highest density region at the final time step, 4.9% of the hydrogen is in H_2 and 0.02% of the carbon is in CO. Note that the abundances of these molecules are still increasing because the H_2 formation timescale is much longer than the collapse timescale $t \simeq 10^5$ yr (see Fig. 1*d*).

3.5. *Thermal Instability of Isobarically Cooling CNM*

Figure 8 shows the evolution of the fluid element which has the maximum density at each time step. The shaded area of Figure 8*b* denotes the thermally unstable region. In this case of linear analysis (Appendix B), chemical compositions in thermal and chemical equilibrium states of each density are used. This figure shows how thermally stable CNM becomes unstable. The growth time of the instability is shown in Figure 9. In Figure 9*b*, we superpose the temperature evolution of our nonlinear calculation (Fig. 7*b*) upon the growth rate contours (Fig. 9*a*). The shortest wavelength of unstable perturbation is $\lambda_{\rm min} \sim 2.5 \times 10^{-5}$ pc ≈ 5 AU.

3.6. *Results from Various Initial Parameters*

Calculations are done at nine different initial densities ($10^{-2} < n < 10^2$) and 11 velocity differences ($2 <$ Mach number < 12). The column density is 10^{20} cm^{-2}. We follow the calculation until $t = 10^5$–10^6 yr. The number fraction of H_2 in the highest density region is shown in Figure 10. The horizontal axis denotes the initial number density of hydrogen nuclei. The vertical axis denotes the velocity difference. Solid lines denote the 8% boundary of the H_2 number fraction. Higher velocity produces more abundance of H_2 in the thermally collapsed layer. Note that the fragmentation of the thermally collapsed layer will change the column density of the fragments, which change the efficiency of H_2 self-shielding. Therefore, the amount of H_2 in the fragments would be different from the value obtained in this paper. To determine the realistic abundance of H_2, two- or three-dimensional hydrodynamic calculation is required.

4. DISCUSSION

Our hydrodynamic calculations show that thermal instability produces the collapsed layer with a considerable

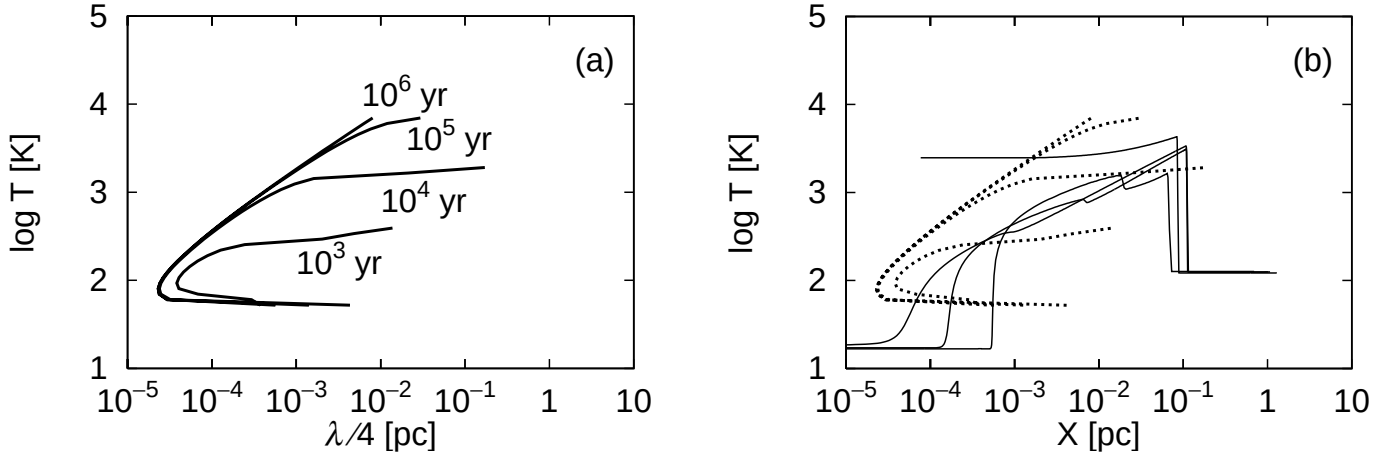

FIG. 9.—Growth time of the instability. The vertical axis denotes unperturbed temperature. The value of the constant pressure, $P_c/k_{\rm B} = 2 \times 10^5$ K cm^{-3}, is adopted from the result of our nonlinear calculation. The density can be deduced from the relation $n = P_c/k_{\rm B}T$. The horizontal axis denotes a quarter of the perturbation wavelength. Contours of growth time are depicted in this wavelength-temperature plane. The shortest wavelength of unstable perturbation is $\lambda_{\rm min} \sim 2.5 \times 10^{-5}$ pc ≈ 5 AU. (*b*) We superpose the temperature evolution of our nonlinear calculation (Fig. 7*b*) upon the growth rate contours shown in panel *a*.

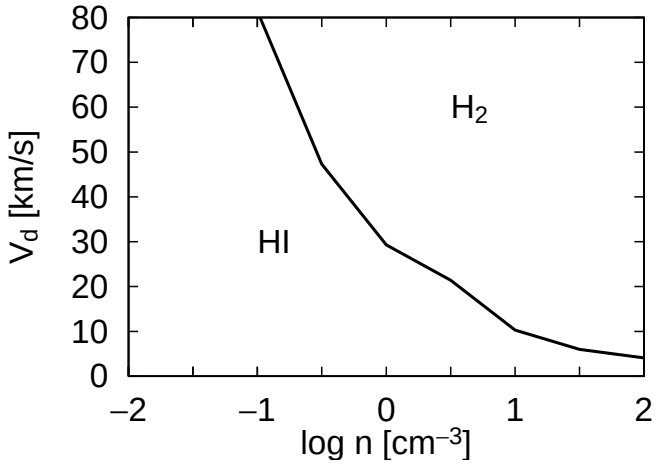

FIG. 10.—Chemical abundance of the thermally collapsed layers in the one-dimensional hydrodynamic calculation. The horizontal axis denotes the initial number density. The vertical axis denotes the velocity difference. The solid line denotes the 8% boundary of the H_2 number fraction.

amount of H_2. In this section, we discuss the consequence of this instability.

4.1. *Fragmentation of the Thermally Collapsed Layer*

The shock propagation into the ISM can produce the thermally collapsing gas inside the shock-compressed layer. The initial thickness of the thermally collapsed layer is dozens of AU and agrees with the prediction by the linear analysis. The thickness of the thermally collapsed layer increases with time through the accretion of gas. The thermally collapsing layer is dynamically unstable also in the y- and z-directions, so that perturbations in the layer will grow and lead to fragmentation of the layer. We expect that this layer will break up into very small cloudlets which have different translational velocities. This velocity dispersion of cloudlets produced by the passage of supernova shocks may be an origin for the observed interstellar "turbulent" velocities. Extremely high pressure in the tiny-scale structure observed in H I clouds (Heiles 1997) is consistent with our shock propagation model.

4.2. *Molecular Clouds in the Galaxy*

It seems difficult to detect these cloudlets in emission lines of CO molecules (see, e.g., Liszt & Wilson 1993; Liszt 1994). Many shell-like or filamentary structures in the H I 21 cm observation maps (Hartmann & Burton 1997) are reminiscent of overlapping shells of old SNRs. If these structures in H I maps are really the results of SNR shocks, many tiny molecular cloudlets should be hidden in the shell and should be ubiquitous in the Galaxy. McKee & Ostriker (1977) showed that the recycling SNRs in the Galaxy would overlap before they are dissipated. The overlapping filamentary region may produce larger clouds.

5. SUMMARY

We have done one-dimensional hydrodynamic calculations for the propagation of a strong shock wave into WNM and CNM, including detailed thermal and chemical processes. Our results show that the shock propagation into WNM can produce a thin and dense H_2 layer by the thermal instability inside the shock-compressed layer. The shock propagation into CNM can also produce the thermally collapsed layer. We predict that this thermally collapsed layer will fragment into small molecular cloudlets. Our subsequent work, which includes two- or three-dimensional calculations, aims to explore how these cloudlets have velocity dispersion and form larger clouds.

We are grateful to the anonymous referee for helpful comments, which have improved the manuscript. We would like to thank Shoken M. Miyama for discussions and continuous encouragement.

APPENDIX A

THERMAL PROCESSES

In this appendix, thermal and chemical processes in our calculations are summarized. We include the formation and cooling of H_2 and CO in addition to the processes described by W95.

A1. HEATING AND COOLING PROCESSES

A1.1. *Photoelectric Heating from Small Grains and PAHs*

The photoelectric emission from small grains and PAHs induced by FUV photons is an important mechanism for heating a diffuse interstellar gas cloud. We use the results of Bakes & Tielens (1994, hereafter BT) to calculate the photoelectric heating. In their model, grains are distributed with a Mathis, Rumpl, & Nordsieck (1977, hereafter MRN) power-law distribution in size, $n(a)da \propto a^{-3.5}da$, between 3 and 100 Å in radius. BT calculated the charge distribution for each particle size taking the photoionization and the electron and positive ion recombination into account and found the total photoelectric heating from the distribution of particles. The resulting heating rate is given by

$$\Gamma_{pe} = 1.0 \times 10^{-24} \epsilon G_0 \text{ ergs s}^{-1}, \tag{A1}$$

where ϵ is the heating efficiency and G_0 is the incident FUV field normalized to the local interstellar value ($=1.6 \times 10^{-3}$ ergs $\text{cm}^{-2}\ \text{s}^{-1}$) estimated by Habing (1968). BT provide a simple fit to ϵ as a function of $G_0\, T^{1/2}/n_e$:

$$\epsilon = \frac{4.9 \times 10^{-2}}{1.0 + [(G_0\, T^{1/2}/n_e)/1925]^{0.73}} + \frac{3.7 \times 10^{-2}(T/10^4)^{0.7}}{1.0 + [(G_0\, T^{1/2}/n_e)/5000]}, \tag{A2}$$

where n_e is the electron density.

Grains and PAHs may also be important gas coolants. We treat the heating caused by the electron ejection (eq. [A1]) and the recombination cooling separately, so that the net heating or cooling is the difference between the heating and cooling. We use the fit to the recombination cooling provided by BT:

$$\Lambda_{\rm pe} = 4.65 \times 10^{-30} T^{0.94} (G_0\, T^{1/2}/n_e)^{\beta} n_e \ \text{ergs s}^{-1}\ , \tag{A3}$$

with $\beta = 0.74/T^{0.068}$.

A1.2. *Ionization Heating by Cosmic Rays and Soft X-Rays*

When the UV flux is strongly attenuated by hydrogen photoabsorption, cosmic rays provide a main heating mechanism. We adopt a primary cosmic-ray ionization rate of $\zeta_{\rm CR} = 1.8 \times 10^{-17}$ s^{-1} (including the ionization of He) following W95. Primary electrons ejected by cosmic-ray ionization have a larger kinetic energy than that of thermal electrons. This primary electron heats surrounding gas by secondary ionization. The total heating rate is given by

$$\Gamma_{\rm CR} = \zeta_{\rm CR}\, E_h(E,\, x_e)\ , \tag{A4}$$

where the function $E_h(E,\, x_e)$ gives the heat deposited for each primary electron of energy E (Shull & Van Steenberg 1985).

Soft X-rays also ionize and heat the ISM. W95 calculated the heating and ionization rates using the observed diffuse X-ray spectrum and photoionization cross section of H, He, and other trace elements. The analytic fits are given in their paper. Soft X-ray is attenuated by photoabsorption of neutral hydrogen atom. We use the value of the absorbing column density 10^{19}–10^{20} cm^{-3} as a standard H I cloud.

A1.3. *Formation and Photodissociation Heating from* H_2

When a hydrogen molecule is photodissociated, the chemical potential of the gas is raised by the dissociation energy, 4.48 eV. In addition to this, a small amount of kinetic energy is deposited to the photodissociated atoms. According to Hollenbach & McKee (1979, hereafter HM79), the heating rate is

$$\Gamma_{\rm UV} = 9 R_{\rm pump} \{(2.2\ \text{eV})[1 + n_{\rm cr}({\rm H}_2)/n]^{-1}\}\ , \tag{A5}$$

where

$$n_{\rm cr} = \frac{10^6 T^{-1/2}}{1.6 x_{\rm H} \exp\,[-(400/T)^2] + 1.4 x_2 \exp\,\{-[12000/(T + 1200)]\}}\ \text{cm}^{-3} \tag{A6}$$

and the rate coefficient $R_{\rm pump}$ is given in § A2.2.

When a hydrogen molecule forms through associative detachment or catalytic reaction, it is in a highly excited rovibrational state. Only a small fraction of the formation energy is available for heating the gas, while most of the energy escapes the cloud via line emission. We use the heating rates from HM79 as follows:

$$\Gamma_{\rm gr} = R x_{\rm H} \{0.2 + 4.2[1 + n_{\rm cr}({\rm H}_2)/n]^{-1}\}\ , \tag{A7}$$

and the rate coefficient R is given in § A2.2.

A1.4. *Atomic Line Cooling*

At high temperatures ($T \gtrsim 8000$ K) collisional excitation of hydrogen Lyα can contribute to the cooling. We also include low-lying metastable transitions of C II (2326 Å), O I (6300 Å), Fe II (5.3 μm), and Si II (2240 Å), using rates from Hollenbach & McKee (1989, hereafter HM89).

Collisional excitation of the fine-structure lines of C II (158 μm) and O I (63 μm) is a dominant gas coolant at temperatures $T \lesssim 8000$ K. Additional cooling is provided by the fine-structure transitions of the ground electronic state of Fe II (26 μm), Si II (35 μm) (HM89).

We adopt trace element abundance following W95: $x_{\rm He} = 0.1$, $x_{\rm O} = 4.6 \times 10^{-4}$, $x_{\rm C} = 3 \times 10^{-4}$, $x_{\rm Si} = 3.55 \times 10^{-6}$, and $x_{\rm Fe} = 7.08 \times 10^{-7}$. Several trace elements, C, Si, and Fe, have ionization potentials less than 13.6 eV and thus are susceptible to ionization by the interstellar UV field. For convenience, the level of ionization of these trace elements is assumed to be singly charged. On the other hand, oxygen remains neutral by charge exchange reaction to hydrogen because oxygen has almost the same ionization potential as hydrogen.

A1.5. H_2 *Cooling*

At temperatures above 500 K, rovibrational lines of H_2 contribute to the cooling function. Following HM79 we adopt

$$\Lambda_{\rm H_2} \approx n({\rm H}_2)\left[x_{\rm H} \frac{L_{\rm vr}^{\rm H}({\rm LTE})}{1 + n_{\rm cr}^{\rm H}/n} + x_2 \frac{L_{\rm vr}^{\rm H_2}({\rm LTE})}{1 + n_{\rm cr}^{\rm H_2}/n}\right], \tag{A8}$$

where $n_{\rm cr}$ is the critical density defined as follows:

$$n_{\rm cr}^{\rm H,H_2} \equiv \frac{L_{\rm vr}^{\rm H,H_2}({\rm LTE})}{L_{\rm vr}^{\rm H,H_2}(n \to 0)}\, n\ , \tag{A9}$$

which depends on temperature only, not on density. We use the function $L_{\rm vr}^{\rm H,H_2}({\rm LTE})$, $L_{\rm vr}^{\rm H,H_2}(n \to 0)$ from HM79. We update the function $L_r^{\rm H}(n \to 0)$ from Galli & Palla (1998). We assume an ortho-H_2–to–para-H_2 ratio of 3:1.

A1.6. CO *Cooling*

Rotational line emission from CO is a major low-temperature cooling agent for molecular clouds. The CO rotational cooling is derived from McKee et al. (1982). The optically thin cooling function is

$$\Lambda_{\rm CO}({\rm rot}) = \frac{4(k_{\rm B}T)^2 A_0}{E_0[1 + (n_{\rm cr}/n) + 1.5(n_{\rm cr}/n)^{1/2}]}\,, \tag{A10}$$

where $A_0 = 9.7 \times 10^{-8}\ {\rm s}^{-1}$, $E_0/k_{\rm B} = 2.76$ K, $n_{\rm cr} = 3.3 \times 10^6 T_3^{3/4}\ {\rm cm}^{-3}$ for ^{12}CO (McKee et al. 1982).

The CO vibrational cooling at the lowest level is

$$\Lambda_{\rm CO}({\rm vib}) = \sum_{\rm H,H_2} \gamma_{01}^{\rm H,H_2}\,\Delta E_{10}\,, \tag{A11}$$

where $\Delta E_{10} = 3080\ {\rm K}/k_{\rm B}$. The vibrational rate coefficients for transitions to the $v = 1$ state of CO were taken from HM89.

A1.7. *Atomic and Molecular Collisions with Dust Grains*

The cooling of the gas by cooler dust grains is important at high densities $n \gtrsim 10^5\ {\rm cm}^{-3}$. The cooling rate per hydrogen nucleus is

$$\Lambda_{\rm gr} = 1.2 \times 10^{-31} n \left(\frac{T}{1000\ {\rm K}}\right)^{1/2} \left(\frac{100\ {\rm \AA}}{a}\right)^{1/2} \times \left[1 - 0.8\ \exp\left(\frac{-75}{T}\right)\right](T - T_{\rm gr})\ {\rm ergs\ s}^{-1}\,, \tag{A12}$$

where $T_{\rm gr}$ is an effective grain temperature, averaged over the assumed MRN size distribution (HM89). Since the gas generally collides with the smaller grains, we take $T_{\rm gr}$ to be the temperature 8 K of grains of radius $a = 100$ Å.

A2. CHEMICAL REACTIONS

For the range of temperatures and densities considered, the recombination timescale is longer than the cooling timescale (see Fig. 1*d*). The residual electrons make the cooling rates larger than that of equilibrium abundance. Therefore, it is imperative to treat chemical nonequilibrium processes.

The main coolant in dense clouds is supposed to be CO, so that CO formation should be taken into account. Although H_2 is a minor coolant, H_2 enables the formation of CO. Thus, we should take into account the formation of H_2.

A2.1. *Ionization and Recombination of the Hydrogen Atom*

Photoionizing UV fields are attenuated by a large absorption cross section of hydrogen atoms. The hydrogen atoms are also ionized by cosmic rays and X-rays. The total ionization rates per hydrogen atom are given in the appendix of W95. Collisional ionization is also important in shock-compressed layers, and the rate coefficient of this processes is $k_I = 5.8 \times 10^{-9} T_4^{0.50} \exp(-15.8/T_4)\ {\rm cm}^{-3}\ {\rm s}^{-1}$ (HM79). The radiative recombination coefficient of hydrogen is given by Shapiro & Kang (1987).

A2.2. *Formation and Dissociation of* H_2

H_2 is formed catalytically on dust grains and by associative detachment; it is destroyed by collisional dissociation, by photodissociation via the Lyman-Werner electronic transitions, and by cosmic rays.

Following Tielens & Hollenbach (1985, hereafter TH85), the rate at which H_2 is produced catalytically on dust grains is

$$R = 0.5 \bar{v} n_{\rm H} n_d \sigma_d S(T) \approx 6 \times 10^{-17} (T/300)^{0.5} n_{\rm H} n S(T)\ {\rm cm}^{-3}\ {\rm s}^{-1}\,, \tag{A13}$$

$$S(T) = [1 + 0.04(T + T_{\rm gr})^{0.5} + 2 \times 10^{-3} T + 8 \times 10^{-6} T^2]^{-1}\,, \tag{A14}$$

where $\bar{v}$ is the mean thermal velocity of the atomic hydrogen, n_d is the number density of dust grains, and σ_d is the average dust grain cross section.

H_2 can be formed by associative detachment of the H^- ion,

$$H + H^- \rightarrow H_2 + e^-\,. \tag{A15}$$

We use the formation rates from HM79 to obtain an effective rate coefficient.

The shock waves can produce sufficiently high temperatures so that collisional dissociation of H_2 should be considered. The rate of dissociation of H_2 by H atoms is $k_D = 3.4 \times 10^{-9} \exp(8000/T) \exp(-5.19 \times 10^4/T)\ {\rm cm}^{-3}\ {\rm s}^{-1}$ (HM79). The rate of dissociation of H_2 by electron impact with LTE vibrational population is taken into account (Stibbe & Tennyson 1999). Although these LTE reaction rates are overestimates for H_2 dissociation, there is no significant difference between models with and without collisional dissociation. H_2 forms after the gas layer collapses because the timescale of H_2 formation is much larger than cooling timescale. The temperature in the collapsed layer is too low for H_2 to dissociate by collision. This is why collisional dissociation is ineffective in our models.

We adopt the rate of photodissociation from TH85,

$$R_{\rm pump} = 3.4 \times 10^{-10} G_0\, \beta(\tau)\ {\rm s}^{-1}\,, \tag{A16}$$

where $\beta(\tau)$ is the probability that photons of the interstellar radiation field penetrate to optical depth τ in a plane-parallel cloud layer. Photodissociating UV fields are self-shielded by H_2, and the optical depth τ is

$$\tau = 1.2 \times 10^{-14} N({\rm H_2}) \delta V_D^{-1}\,, \tag{A17}$$

where $N(H_2)$ is the column density of H_2 and δV_D is the Doppler line width in kilometers per second, and we adopt this value to be the sound velocity. The analytic expression of $\beta(\tau)$ is given by TH85.

The rate at which cosmic rays destroy H_2 is estimated by HM89 to be $2.29\zeta_{CR}$, where ζ_{CR} is the primary cosmic-ray ionization rate for atomic hydrogen.

A2.3. *Carbon Chemistry*

We include a simplified treatment of the conversion of singly ionized carbon C^+ to carbon monoxide CO following Langer (1976) and Nelson & Langer (1997). The simplified chemical model assumes the direct conversion of C^+ to CO, or vice versa, without accounting explicitly for the intermediate reactions. The equation describing the rate of production and destruction of CO is written as

$$\frac{dn(\mathrm{CO})}{dt} = k_0\, n(\mathrm{C}^+) n\beta - \Gamma_{\mathrm{CO}}\, n(\mathrm{CO})\,, \tag{A18}$$

where $k_0 = 5 \times 10^{-16}\ \mathrm{cm^3\ s^{-1}}$, $\Gamma_{\mathrm{CO}} = 10^{-10} G_0\ \mathrm{s^{-1}}$, and β is defined by the expression

$$\beta = \frac{k_1\, x(\mathrm{O\ I})}{k_1\, x(\mathrm{O\ I}) + G_0[\Gamma_{\mathrm{CH}x}/n(\mathrm{H}_2)]}\,. \tag{A19}$$

The definition of $\Gamma_{\mathrm{CH}x}$ is given by $\Gamma_{\mathrm{CH}x} = 5 \times 10^{-10} G_0$, and k_1 takes the value $k_1 = 5 \times 10^{-10}$. For CO photodissociation we do not treat the line self-shielding of CO following Nelson & Langer (1997) because we are only interested in the beginning of CO formation.

APPENDIX B

THERMAL INSTABILITY IN ISOBARICALLY CONTRACTING GAS

To study the characteristic length and timescale of the thermally collapsed layer, we have done linear stability analysis. Field (1965) analyzed the stability of uniform gas in thermal equilibrium. Schwarz, McCray, & Stein (1972) analyzed the isochorically cooling gas without heating. Our nonlinear calculation, however, shows that the shock-compressed layer is almost isobaric. In this appendix, we analyze the stability of isobarically contracting gas.

B1. THE BASIC EQUATIONS

We consider the gas with number density n, temperature T, velocity v, and pressure P, where all variables are functions of position and time. The governing hydrodynamic equations are

$$\frac{dn}{dt} + n\,\frac{\partial v}{\partial X} = 0\,, \tag{B1}$$

$$m_{\mathrm{H}}\, n\,\frac{dv}{dt} = -\frac{\partial P}{\partial X}\,, \tag{B2}$$

$$\frac{1}{\gamma - 1}\,\frac{dP}{dt} - \frac{\gamma}{\gamma - 1}\,\frac{P}{n}\,\frac{dn}{dt} = n\Gamma - n\Lambda + \frac{\partial}{\partial X}\left(K\,\frac{\partial T}{\partial X}\right), \tag{B3}$$

$$P = nk_{\mathrm{B}}\, T\,. \tag{B4}$$

In this analysis, we neglect He atoms for simplicity. The effect of chemical evolution can be included in the nonequilibrium cooling and heating function. For the range of temperatures and densities considered, the chemical timescale is longer than the cooling timescale. We use the nonequilibrium chemical fraction just after shock heating.

B2. THE UNPERTURBED STATE

To express isobarically contracting background, we use the comoving coordinate x related to the real coordinate X,

$$x = X/a(t)\,, \tag{B5}$$

where $a(t)$ is the contraction parameter. In these contracting coordinates, the velocity field can be written as

$$v = \dot{a}x + v_1\,, \tag{B6}$$

where v_1 is the perturbed velocity relative to the contraction.

Lagrangian differentiation of physical variable f is

$$\frac{df}{dt} = \frac{\partial f}{\partial t} + \left(v\,\frac{\partial}{\partial X}\right) f = \left(\frac{\partial f}{\partial t}\right)_x + \frac{1}{a}\left(v_1\,\frac{\partial}{\partial x}\right) f\,. \tag{B7}$$

In comoving coordinates, the one-dimensional hydrodynamic equations are

$$\dot{n} + \frac{\dot{a}}{a} n + \frac{1}{a} \frac{\partial}{\partial x} (n v_1) = 0 , \tag{B8}$$

$$\ddot{a} x + \dot{v}_1 + \frac{\dot{a}}{a} v_1 + \frac{1}{a} \left(v_1 \frac{\partial}{\partial x} \right) v_1 + \frac{1}{m_H n a} \frac{\partial P}{\partial x} = 0 , \tag{B9}$$

$$\dot{P} + \frac{1}{a} \left(v_1 \frac{\partial}{\partial x} \right) P - \gamma \frac{P}{n} \left[\dot{n} + \frac{1}{a} \left(v_1 \frac{\partial}{\partial x} \right) n \right] + (\gamma - 1)(n\Lambda - n\Gamma) = \frac{\gamma - 1}{a^2} \frac{\partial}{\partial x} \left(K \frac{\partial T}{\partial x} \right) . \tag{B10}$$

If we set the perturbed velocity v_1 equal to zero in the above equations, the equations governing the isobarically contracting background are

$$\dot{n} + \frac{\dot{a}}{a} n = 0 , \tag{B11}$$

$$\ddot{a} x + \frac{1}{m_H n a} \frac{\partial P_0}{\partial x} = 0 , \tag{B12}$$

$$\gamma \frac{\dot{a}}{a} + (\gamma - 1) \frac{\Lambda - \Gamma}{k_B T} = 0 . \tag{B13}$$

Equation (B11) leads $n \propto a^{-1}$. Temperature is proportional to a because unperturbed gas is isobaric. From equation (B13), we obtain the approximate solution for $a(t)$ as

$$a(t) = a(0)(1 - t/\gamma \tau_{net}) , \tag{B14}$$

where τ_{net} is a net cooling time defined by $\tau_{net}^{-1} = (\gamma - 1)(\Lambda - \Gamma)/k_B T$. This approximation is valid as long as variations of density and temperature remain small, i.e., $0 < t \ll \gamma \tau_{net}$. Equation (B12) gives $\partial P_0/\partial x = 0$. Thus, we consider a uniform unperturbed state, $\partial n_0/\partial x = 0$. The isobarically cooling gas is characterized by a temperature $T_0(t)$ and a number density $n_0(t)$ which are functions of time, while the pressure P_0 is constant.

B3. THE LINEARIZED EQUATIONS

We now examine the effect of small perturbations:

$$n(x, t) = n_0(t)(1 + n_1(t) \exp (i\kappa x)) , \tag{B15}$$

$$P(x, t) = P_0(1 + P_1(t) \exp (i\kappa x)) , \tag{B16}$$

$$T(x, t) = T_0(t)(1 + T_1(t) \exp (i\kappa x)) , \tag{B17}$$

$$v_1(x, t) = v_1(t) \exp (i\kappa x) . \tag{B18}$$

The first-order equations for T_1, P_1, n_1, and v_1 are

$$\dot{n}_1 + \frac{i\kappa}{a} v_1 = 0 , \tag{B19}$$

$$\dot{v}_1 + \frac{\dot{a}}{a} v_1 + c_s^2 \frac{i\kappa}{a} P_1 = 0 , \tag{B20}$$

$$\dot{P}_1 + \frac{\dot{a}}{a} P_1 - \gamma \dot{n}_1 + \frac{n_1}{\tau_{net}} + \frac{s_T T_1 + s_\rho n_1}{\tau_{cool}} - \frac{r_T T_1 + r_\rho n_1}{\tau_{heat}} = -l c_s \frac{\kappa^2}{a^2} T_1 , \tag{B21}$$

$$P_1 = n_1 + T_1 , \tag{B22}$$

where

$$s_T = \partial \ln \Lambda / \partial \ln T , \tag{B23}$$

$$s_\rho = \partial \ln \Lambda / \partial \ln n , \tag{B24}$$

$$r_T = \partial \ln \Gamma / \partial \ln T , \tag{B25}$$

$$r_\rho = \partial \ln \Gamma / \partial \ln n , \tag{B26}$$

$$\tau_{cool}^{-1} = (\gamma - 1)\Lambda / k_B T , \tag{B27}$$

$$\tau_{heat}^{-1} = (\gamma - 1)\Gamma / k_B T . \tag{B28}$$

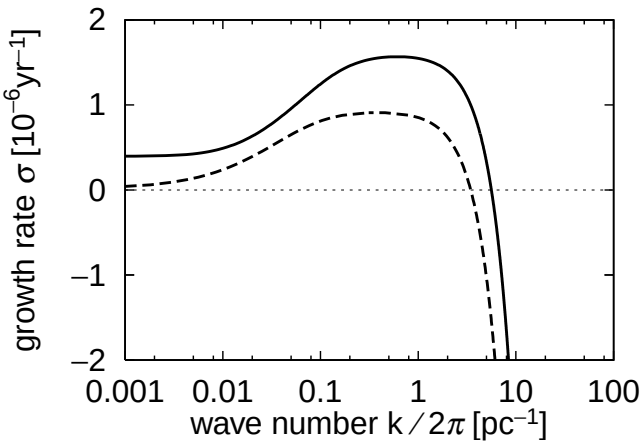

FIG. 11.—Dispersion relation for the condensation mode of the isobarically contracting uniform gas with $n = 10^{0.25}$, $T = 10^{3.0}$ (*solid line*). The case of thermal equilibrium unperturbed state is also shown (*dashed line*).

We adopt the collision mean free path, l, instead of thermal conduction coefficient $K = nk_B lc_s/(\gamma - 1)$. The term $\dot{a}/a$ remains constant ($-1/\gamma\tau_{\rm net}$) as long as $t \ll \gamma\tau_{\rm net}$. We assume that the perturbation is proportional to $\exp(\sigma t)$ and obtain the dispersion relation as

$$\left[\sigma^2 - \frac{2\sigma}{\gamma\tau_{\rm net}} + (kc_s)^2\right]\left(\sigma + \frac{s_T - 1}{\tau_{\rm cool}} - \frac{r_T - 1}{\tau_{\rm heat}} + lc_s k^2\right) - (kc_s)^2\left[(1-\gamma)\sigma + \frac{s_\rho}{\tau_{\rm cool}} - \frac{r_\rho}{\tau_{\rm heat}}\right] = 0\,, \tag{B29}$$

where $k = \kappa/a$. This cubic equation for σ has a real root and two complex conjugate roots. The former root is called condensation mode, and the latter roots are called wave mode. Following Field (1965), we call the most unstable mode the condensation mode. In Figure 11, we show an example of the dispersion relation of the condensation mode.

REFERENCES

Bakes, E. L. O., & Tielens, A. G. G. M. 1994, ApJ, 427, 822
Cox, D. P., & Smith, B. W. 1974, ApJ, 189, L105
Dieter, N. H., Welch, W. J., & Romney, J. D. 1976, ApJ, 206, L113
Field, G. B. 1965, ApJ, 142, 531
Field, G. B., Goldsmith, D. W., & Habing, H. J. 1969, ApJ, 155, L149
Frail, D. A., Weinberg, J. M., Cordes, J. M., & Mathers, C. 1994, ApJ, 436, 144
Galli, D., & Palla, F. 1998, A&A, 335, 403
Habing, H. J. 1968, Bull. Astron. Inst. Netherlands, 19, 421
Hartmann, D., & Burton, W. B. 1997, Atlas of Galactic Neutral Hydrogen (Cambridge: Cambridge Univ. Press)
Heiles, C. 1997, ApJ, 481, 193
Hollenbach, D., & McKee, C. F. 1979, ApJS, 41, 555
———. 1989, ApJ, 342, 306
Langer, W. D. 1976, ApJ, 206, 699
Langer, W. D., Velusamy, T., Kuiper, T. B. H., Levin, S., & Olsen, E. 1995, ApJ, 453, 293
Liszt, H. S. 1994, ApJ, 429, 638
Liszt, H. S., & Wilson, R. W. 1993, ApJ, 403, 663
Mathis, J. S., Rumpl, W., & Nordsieck, K. H. 1977, ApJ, 217, 425
McKee, C. F., & Ostriker, J. P. 1977, ApJ, 218, 148
McKee, C. F., Storey, J. W. V., Watson, D. M., & Green, S. 1982, ApJ, 259, 647
Meyer, D. M., & Blades, J. C. 1996, ApJ, 464, L179
Nelson, R. P., & Langer, W. D. 1997, ApJ, 482, 796
Parker, E. N. 1953, ApJ, 117, 431
Shapiro, P. R., & Kang, H. 1987, ApJ, 318, 32
Schwarz, J., McCray, R., & Stein, R. 1972, ApJ, 175, 673
Shull, J. M., & McKee, C. F. 1979, ApJ, 227, 131
Shull, J. M., & van Steenberg, M. E. 1985, ApJ, 298, 268
Smith, J. 1980, ApJ, 238, 842
Stibbe, D. T., & Tennyson, J. 1999, ApJ, 513, L147
Tielens, A. G. G. M., & Hollenbach, D. 1985, ApJ, 291, 722
Truelove, J. K., Klein, R. I., McKee, C. F., Holliman, J. H., II., Howell, L. H., Greenough, J. A., & Woods, D. T. 1998, ApJ, 495, 821
van Leer, B. 1997, J. Comput. Phys., 135, 229
Wolfire, M. G., Hollenbach, D., McKee, C. F., Tielens, A. G. G. M., & Bakes, E. L. O. 1995, ApJ, 443, 152